Cell Reports
Physical Science

CellPress
OPEN ACCESS

Article

Umbrella evaporator for continuous solar vapor generation and salt harvesting from seawater

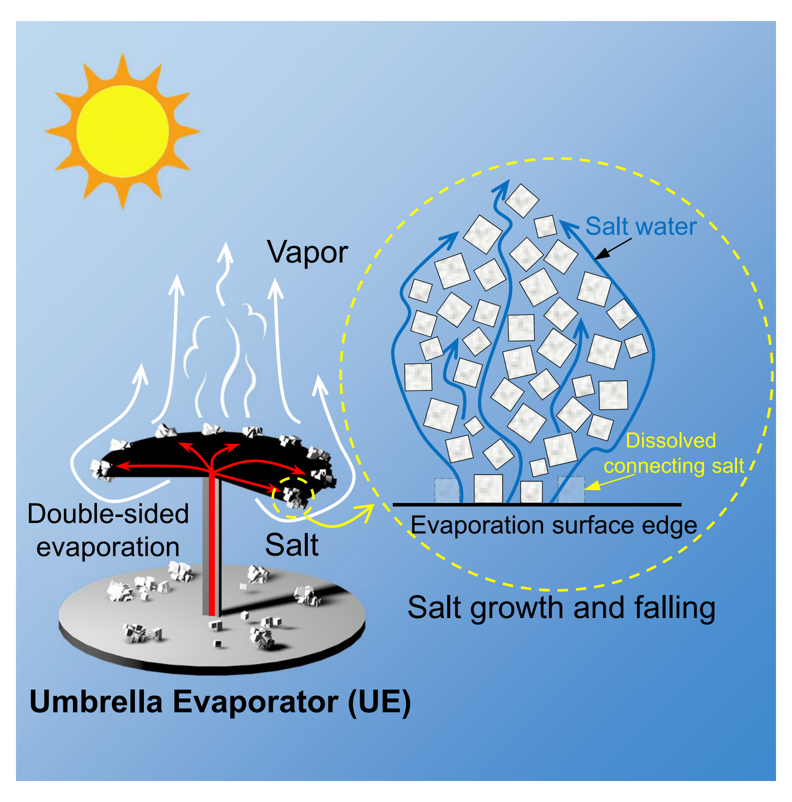

Solar evaporation could mitigate water stress problems, but challenges remain in structural improvement of devices, salt accumulation, and salt harvesting mechanisms. Ma et al. show an umbrella evaporator that achieves efficient vapor generation and salt harvesting concurrently via double-sided evaporation and reveal the salt nucleation, growth, and falling mechanism of salt harvesting.

Xiaolong Ma, Xiaodong Jia,
Guice Yao, Dongsheng Wen

d.wen@leeds.ac.uk, d.wen@buaa.edu.cn

Highlights

Umbrella evaporator achieves a high efficiency via double-sided evaporation

Central water supply results in salt accumulation at edges

Salt grows from the front by wicking water through its porous structures

Salt creeping behaviors indicate if Ca^{2+} and Mg^{2+} content is below the lower limit

Ma et al., Cell Reports Physical Science *3*, 100940
July 20, 2022 © 2022 The Author(s).
https://doi.org/10.1016/j.xcrp.2022.100940

Cell Reports
Physical Science

CellPress
OPEN ACCESS

Article

Umbrella evaporator for continuous solar vapor generation and salt harvesting from seawater

Xiaolong Ma,[1] Xiaodong Jia,[1] Guice Yao,[2] and Dongsheng Wen[1,2,3,4,*]

SUMMARY

Solar vapor generation, which uses photothermal materials to desalinate seawater by evaporation, is a promising technology to mitigate the water scarcity problem, but its performance is hindered by large heat leak and salt accumulation problems. Here we report an umbrella evaporator that achieves efficient vapor generation and salt harvesting concurrently via double-sided evaporation and reveal the salt nucleation, growth, and falling mechanism. The evaporator reaches an evaporation rate of 1.25 kg $m^{-2}\cdot h^{-1}$ under ambient conditions, and its continuous operation for vapor and salt production from seawater is demonstrated. The salt mobility on the evaporation surface determines whether the salt could accumulate at the edge, which is influenced by water supply, solar intensity, salinity, and Mg^{2+} and Ca^{2+} contents.A simple salt creeping test on a glass slide is developed to determine whether and to what extent seawater needs to be pre-treated for continuous operation.

INTRODUCTION

Nowadays, one in three people do not have access to safe drinking water.[1] By 2050, one-half of our population will be living in water-stressed areas.[2] Solar vapor generation (SVG), which uses photothermal materials to convert solar energy into heat to evaporate water and directly produce drinkable water, is a promising technology to help mitigate the water scarcity problem.[3–7] This evaporation process mainly consists of two steps: vapor generation at the interface and vapor transfer to the gas phase.[8] The photothermal materials aid in vapor generation by increasing solar energy capture at the interface, while the vapor transfer condition is greatly affected by the evaporator structure and the surroundings. In recent years, photothermal materials for SVG are booming,[9–13] with carbon-based, plasmonic, and semiconducting materials being the most widely explored.[14–16] By contrast, the solar evaporator structure study, which is crucial for vapor transfer, still lacks adequate attention.

A typical solar evaporator floats at the water-air interface, which usually has a thermal insulation layer to localize the heat on the evaporation surface, known as an interfacial evaporator (IE).[17–20] However, when applied on real seawater, salt accumulates on the photothermal materials, decreasing its absorption and blocking the water transport channels.[21,22] The accumulated salt gradually slows down the evaporation and finally stops the whole system.[23]

To solve the salt accumulation problem, a series of studies have been conducted, including designing salt back diffusion pathways into the bulk solution,[24–30] employing contactless solar evaporator,[31,32] and rejecting salt crystals back to the bulk water.[21,33] Nevertheless, considering the salt value, salt should not be treated as a waste discharging back to the sea, but a highly added-value product. A ton of

[1] School of Chemical and Process Engineering, University of Leeds, Leeds LS2 9JT, UK

[2] Beihang University, Beijing 100191, P.R. China

[3] Lehrstuhl für Thermodynamik, Technische Universität München, Garching 85748, Germany

[4] Lead contact

*Correspondence:
d.wen@leeds.ac.uk, d.wen@buaa.edu.cn

https://doi.org/10.1016/j.xcrp.2022.100940

seawater contains 35 kg sea salt having a current value of $4.2 (i.e., $120 per ton), while a ton of freshwater equals $2.8 on average for 30 cities in the United States (Database: Statista). Harvesting salt with SVG is the optimal strategy from both environmental and economic perspectives. Some attempts have been made to achieve salt harvesting concurrently by periodically cleaning the evaporation surface manually,[34,35] which decreases the evaporation rate during the salt accumulation period.

Recently, attention is shifted to an umbrella-shaped evaporator.[36–39] It features a central water supply and an edge salt collection, leaving a clean evaporation surface uncovered by salt, which is promising for SVG and salt harvesting concurrently. It adopts similar concepts to the IE, relying on the top surface evaporation with the back surface insulated, and operates well with simple simulated seawater (e.g., a 35 g/L NaCl solution). However, it is unclear how actual seawater affects its continuous operation, and the salt nucleation, growth, and falling mechanism remains poorly understood. Furthermore, the study of the evaporator structure influence on the system efficiency is still insufficient.

Here, we demonstrate an innovative umbrella evaporator (UE), which achieves double-sided evaporation by discarding the thermal insulation layer beneath and improves the efficiencies of both vapor production and salt collection concurrently. We show its advantages in vapor generation over a typical IE by both experiments and simulation. Benefiting from the central water supply design, salt falls down automatically from the edge by gravity. We explore the factors affecting the salt harvesting at the macroscale and reveal the salt nucleation, growth, accumulation, and falling mechanisms at the microscale. Furthermore, we show the hindering roles of Mg^{2+} (especially) and Ca^{2+} in salt harvesting in seawater and propose a facile method to determine if the pretreated seawater can achieve salt falling by observing the salt creeping behaviors on a glass slide. This work demonstrates a promising future of the UE in SVG and salt harvesting concurrently and allows us to better understand and control the salt harvesting process.

RESULTS AND DISCUSSION

Evaporation performance

A typical IE floats at the air-water interface with a thermal insulation layer to localize the heat on the evaporation surface, making it single-sided evaporation (Figure 1A). In addition, seawater supply from the edge accumulates salts at the center, hindering further water supply and evaporation. The UE we propose in this work discards the thermal insulation layer to make it double-sided evaporation in the air. Benefiting from the central seawater supply, salts could precipitate at the edge and fall down for harvesting. First, we compared the evaporation performance of the IE and the UE by experiments in the same test environment using deionized water (Figure 1B). We coated polypyrrole only on a filter paper by ultrasonic spray coating to make the black evaporation surfaces, which was further made into an IE and a UE (Figures 1B, S1 and S2). The solar absorptance of the evaporation surface is 96.2% (Figure S3; Note S1), and the porosity of the surface and the pillar is 0.806 and 0.885, respectively (Note S2). The average ambient temperature is 21.8°C and the ambient relative humidity is 0.5 for the evaporation tests.

In solar evaporation under 1 sun (1 kW/m^2), UE has a much lower surface average temperature (33.8°C) than IE (40.5°C) (Figure 1C), which is caused by a higher

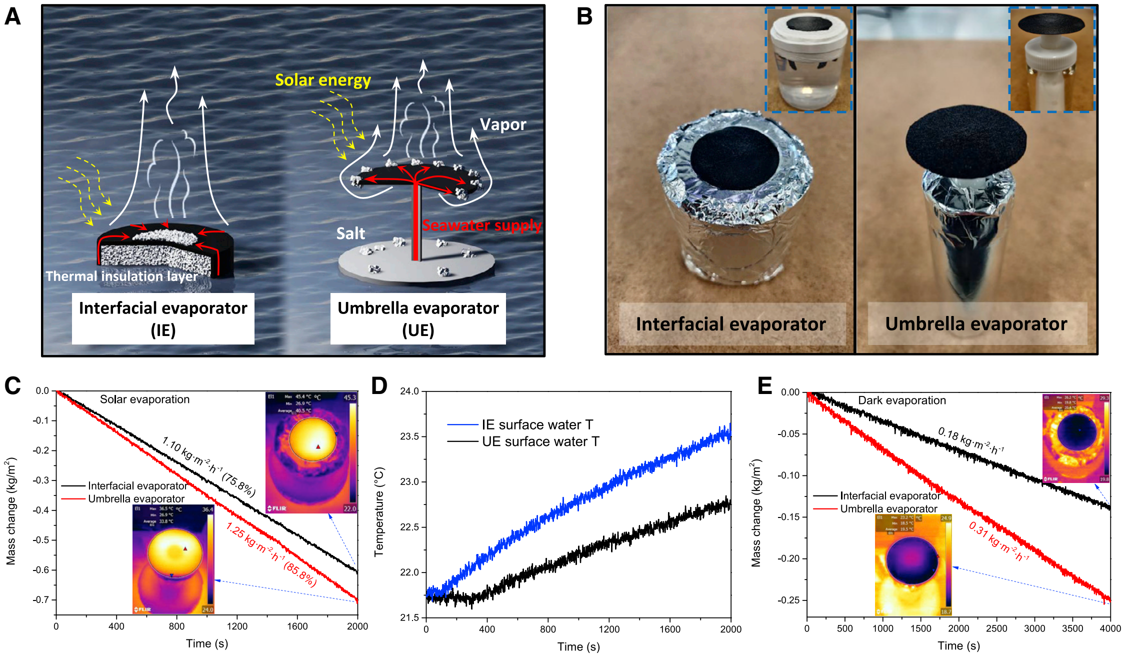

Figure 1. Evaporation performance of the IE and UE

(A) Schematic illustration of the IE and UE.

(B) The IE and UE used for the evaporation test (3 cm in surface diameter).

(C) Solar evaporation under 1 sun (1 kW/m^2).

(D) Surface water temperature in solar evaporation.

(E) Dark evaporation.

evaporation rate (i.e., 1.25 vs. 1.10 kg m^{-2}·h^{-1}, a 13.6% increase). A lower surface temperature would also help to decrease heat loss by decreasing the temperature difference with the environment. A higher evaporation rate and lower surface temperature help to allocate more energy to the evaporation process by decreasing the heat loss to the environment, leading to a higher energy efficiency of the UE (85.8%) than that of the IE (75.8%). As the UE has a lower surface temperature and a smaller heat transfer area to the bulk water, its surface water temperature increased only 0.95°C in 2000 s; by contrast, IE increased more rapidly (by 1.75°C), indicating more heat loss to the bulk water (Figure 1D). The evaporation performance comparison of different reported evaporators is listed in Table S1. It should be noted that the evaporation rate in this work only comes from the surface evaporation without any side wall evaporation. The maximum evaporation rate achieved in this work is 1.25 kg m^{-2}·h^{-1}, which is very close to the theoretical evaporation rate of 1.47 kg m^{-2}·h^{-1} under 1 sun and ambient evaporation temperature.[40] It shall be noted with great caution in evaluating the reported evaporation rates from different evaporators, as shown in Table S1, especially for those values beyond the theoretical limit. This work aims to provide a fair platform to compare the evaporation rate of the IE and UE under the same conditions.

In dark evaporation (i.e., no light), the average temperature of both surfaces (IE 20.4°C and UE 19.5°C) is lower than the environment (21.8°C), indicating that the surfaces obtain energy from the environment, which drives the evaporation (Figure 1E). Owing to double-sided heat capture from the environment, UE has a higher surface average temperature than IE. Combining with the double-sided vapor transfer, the UE has a remarkable 72% higher evaporation rate (0.31 kg m^{-2}·h^{-1}) than that of the IE (0.18 kg

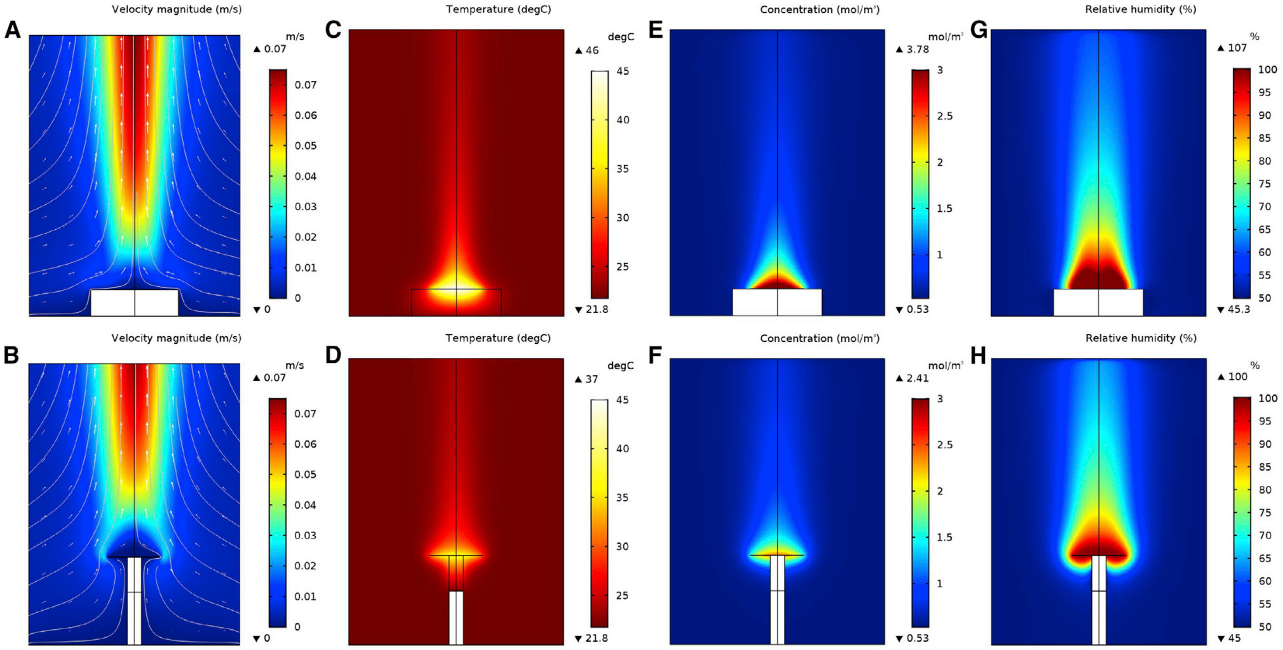

Figure 2. Solar evaporation simulation of IE and UE

(A and B) IE and UE velocity fields.

(C and D) IE and UE temperature fields.

(E and F) IE and UE vapor concentration fields.

(G and H) IE and UE relative humidity fields.

$m^{-2} \cdot h^{-1}$). Therefore, UE has a better SVG performance for both solar and dark evaporation.

To better understand the UE structural advantages in solar evaporation, we simulated the evaporation process by COMSOL Multiphysics. We used a two-dimensional axial symmetry steady-state model to simulate the evaporation system, including all the main processes (fluid flow, heat transfer, and vapor diffusion; details in Figures S4–S7, Tables S2–S5, and Note S3). The simulation domain is 12-cm diameter and 16-cm high cylindrical domain with open boundaries; the evaporation surface is 3 cm in diameter. The velocity field of the IE and the UE is similar: air converges from the periphery over the evaporation surface and then flows up carrying vapor, caused by the density decrease by the solar evaporator heating (Figures 2A and 2B). The temperature of the IE is obviously higher than UE, with the surface central part being the highest for both cases (Figures 2C and 2D). As the surface temperature is far below the boiling point, we support naming this process solar vapor generation instead of solar steam generation.[41] Most of all, the UE vapor concentration and relative humidity fields differ a lot from the IE (Figures 2E–2H). Both sides of the UE surface can evaporate, doubling the mass transfer area. A better mass transfer condition leads to a higher evaporation rate and a lower surface temperature, which increases the energy efficiency.

The pressure and velocity fields of the pillar and the evaporation surface of the UE are displayed in Figure S8. A thermal insulation layer under the UE surface would localize the heat on the surface, but hinder the back evaporation, decreasing the overall evaporation rate (verified by simulation in Figure S9). Therefore, double-sided evaporation of the UE is the key factor to surpass the single-sided IE in evaporation performance.

Energy efficiency improvement

Based on the simulation, we further analyzed the key factors affecting the energy efficiency. The surface diameter is 3 cm and the surface height for UE is 5 cm. Higher ambient temperature, lower ambient humidity, higher bulk temperature, and higher surface solar absorptance all increase the energy efficiency for both UE and IE (Figures 3A–3D). A larger diameter decreases the energy efficiency owing to deteriorated mass transfer conditions (Figure 3E). Specially for the UE, there are two additional factors to consider: the surface height and the opening angle. If the surface is too low (i.e., <3 cm in height for a 3-cm diameter case), the ground surface would affect the back vapor transfer (Figure 3F). The opening angle of the evaporation surface also affects the vapor transfer (Figures 3G and 3H). At the same vertical projected area, a larger opening angle enhances the back vapor transfer especially when the opening angle is greater than 105° (Figure 3I). Meanwhile, smaller or larger opening angles cost more surface area. A flat evaporation surface (opening angle = 90°) reaches the highest evaporation rate per unit surface area (Figure 3I). It should be noted that the UE with any opening angle has a higher evaporation rate than the IE. As demonstrated, the energy conversion efficiency depends on the whole evaporation system.

Salt accumulation and collection

The most attractive feature of the UE is the salt harvesting from the edge.[36] We designed a UE with a saline water supply system to adjust the water level using a communicating vessel (Figure S10). As the water absorption of the filter paper decreases with time, we used a new one for every test to minimize its influence (Figure S11). Water level determines the water supply to the surface. Without a water supply system, the water level decreases with evaporation (from −2 to −7.4 cm to the evaporation surface in 24 h), salt accumulates on the edge and does not fall easily (Figure 4A). The salt falling at the edge is determined by the competition between the evaporation rate and the water supply rate at the edge owing to capillarity, which can be simply controlled by adjusting the solar intensity. When the solar light was turned off (i.e., less evaporation to improve water supply), the accumulated salt began to fall piece by piece, and most of the salt fell down in 30 min. When fixed at −6 cm, there are still large salt blocks hanging at the edge, turning off the light also helped the salt falling; when fixed at −8 cm, the salt ring tends to shrink. The surface diameter influence is similar, which determines the water supply to the edge. When the water level is fixed at −2 cm, the UE with a 3-cm diameter works well (Video S1), and a larger diameter accumulates more salt at the edge (Figure 4B). Improving the water supply by turning the light off, most salts fell in 30 min. When the water supply is sufficient (i.e., −2 cm water level and a 3-cm diameter), prewetting condition (no prewetting, by deionized water, or by a saturated NaCl solution) does not affect the salt collection (Figure 4C). The UE can deal with up to 7 wt % NaCl solution (i.e., 2 times of the seawater concentration), which is the upper limit of the reversed osmosis waste brine concentration owing to hydraulic pressure limitations,[42] indicating UE even has the potential to deal with the reverse osmosis waste brine (Figure 4D).

Salt nucleation, growth, and falling mechanism

We set up a UE under a microscope to study the salt nucleation, growth, and falling mechanism (Figure S12). Initially, NaCl crystallizes from the edge to the center in a flat manner and then some parts hump (Figure 5A). These humps accelerate the dissolution of the small crystals around to make them precipitate on the humps forming three-dimensional structures, which can be explained by Ostwald ripening.[43] Salt crystallization on the evaporation surface is a dynamic equilibrium of crystallization and dissolution, in which way salt moves to the edge (Video S2). When the salt at

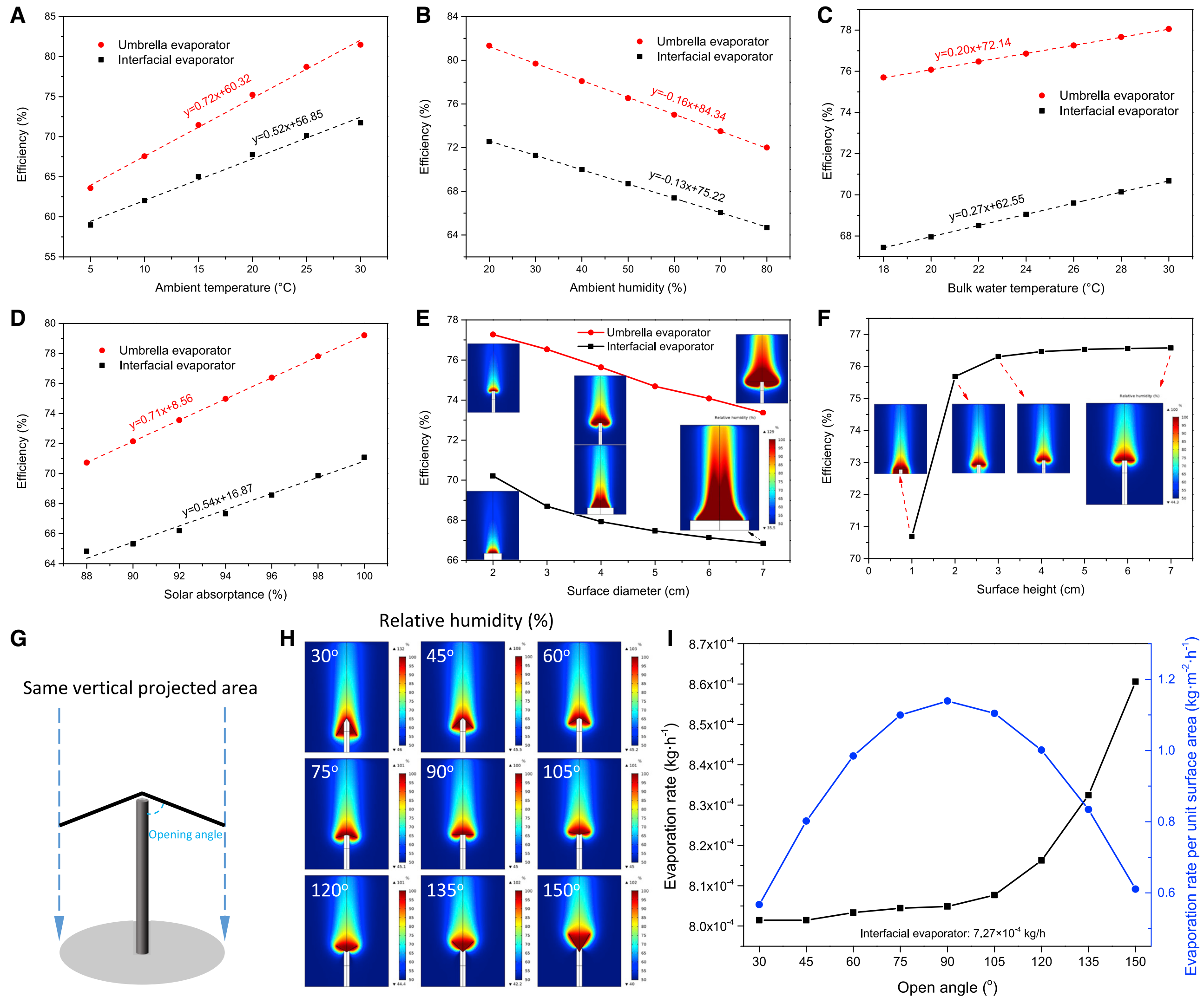

Figure 3. Key factors affecting the energy conversion efficiency

(A) Efficiency versus ambient temperature.

(B) Efficiency versus ambient humidity.

(C) Efficiency versus bulk water temperature.

(D) Efficiency versus solar absorptance of the evaporation surface.

(E) Efficiency versus evaporation surface diameter.

(F) Efficiency versus surface height of the UE.

(G) Schematic of the opening angle and the vertical projected area of the UE.

(H) Influence of the opening angle of the UE on the relative humidity field.

(I) Influence of the opening angle on the overall evaporation rate and the evaporation rate per unit evaporation surface area at the same vertical projected area.

the connecting points is dissolved, salt falls, leaving some tiny seed crystals for the following crystallization. The mobility of the salt determines whether the salt can accumulate at the edge and fall. As above, insufficient water supply, high solar intensity, and high salt concentration will decrease the salt mobility by crystallizing the salt more easily to make the salt gradually precipitate to the center.

Water supply plays an important role in the dynamic equilibrium to harvest salt. It should be noted that salt does not grow from the root pushing forward on the edge, but from

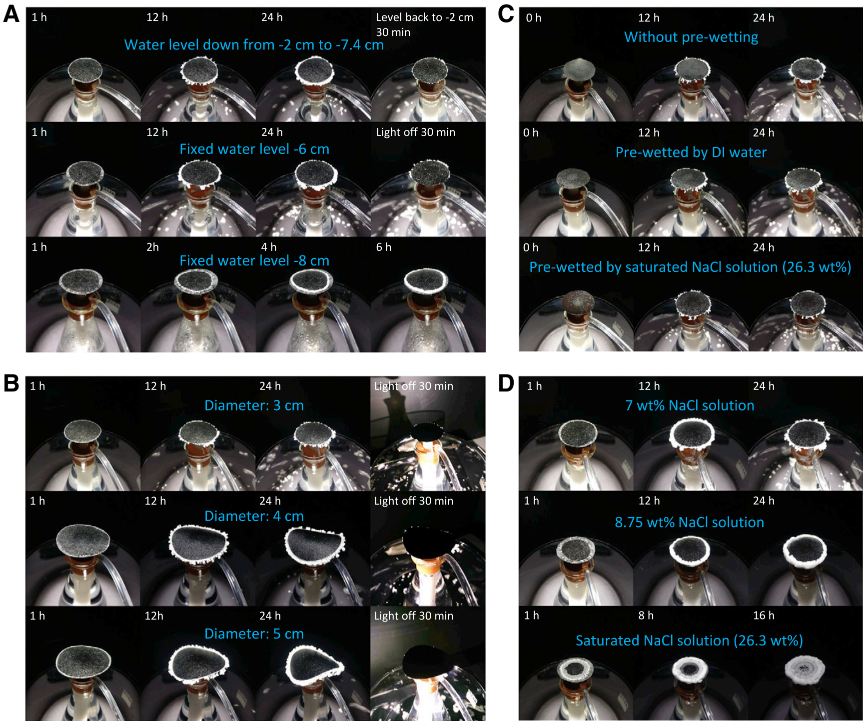

Figure 4. UE salt accumulation and collection performance under different conditions

(A) Water levels.

(B) Evaporation surface diameters.

(C) Prewetting conditions.

(D) Saline water concentrations. All the experiments were conducted under 1 sun with a surface diameter of 3 cm and a surface height of −2 cm in 3.5 wt % NaCl solution. The evaporation surface was pre-wetted by soaking the evaporation surface in 3.5 wt % NaCl solution for 1 min.

the front by wicking the salt water (Video S2). Therefore, the front shape is changing all the time owing to new precipitation (Figure 5B). The porous structures inside the salt clusters supply the water by capillary force,[44] the surface and cross-section of a fallen salt cluster is shown in Figure 5C. Even the fallen salt retains water (Figure 5D). To sum up, salt water is wicked to the front through the channels in the salt clusters, during which the connecting salt is dissolved, leading to the salt falling (Figure 5E).

Application on real seawater

As demonstrated above, the UE works well in both SVG and salt harvesting in the simulated seawater (NaCl solution). However, when applied on real seawater, the evaporation rate decreases and salt gradually covers all the surface without falling (Figure 6A). To find out the reason, we used various simulated seawaters (Table S6). Good salt harvesting performance is still achieved for the basic simulated seawater (NaCl, Na_2SO_4, and KCl) (Figure S13A). The system still works well when Ca^{2+} is added (i.e., 0.41 g/L) (Figure S13B) and stops working at 400% Ca^{2+} (Figure S13G). However, when a small amount of Mg^{2+} is added (even if its 1%), the salt does not fall until the Mg^{2+} is decreased to its 0.1% (Figures S13C–S13F). As a result, Ca^{2+} and Mg^{2+} can both affect salt harvesting, especially Mg^{2+}, which should be decreased below its 0.1% (i.e., 0.0129 g/L).

Based on these findings, we remove Mg^{2+} by adjusting the seawater pH to 12 by NaOH to precipitate $Mg(OH)_2$ ($K_{sp} = 1.5 \times 10^{-11}$), filter the solution, then adjust

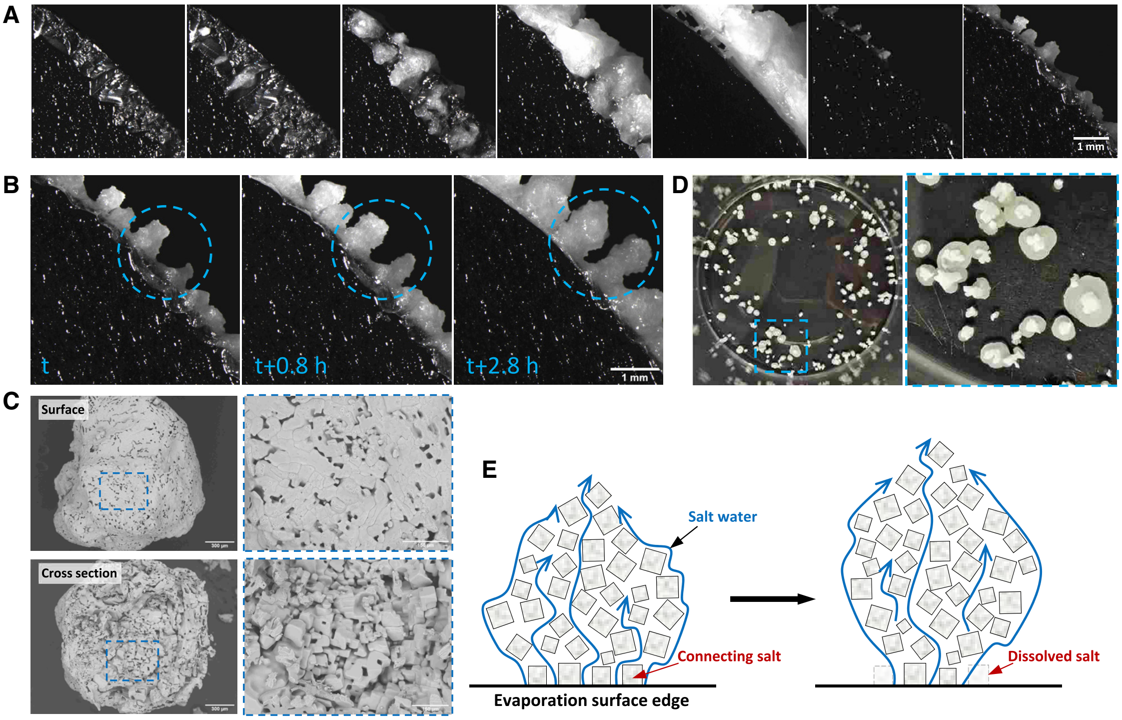

Figure 5. Salt precipitation and falling microscopic behaviors

(A) Salt precipitation and falling microscopic behaviors.

(B) The front shape development of the salt precipitation.

(C) Porous surface and cross-section of a fallen salt cluster.

(D) The fallen salts on the glass and the salt stains.

(E) Salt falling from the edge mechanism schematic.

the pH back to 7 by HCl, and achieved the salt harvesting from the fully simulated seawater (Figure S13H). However, when applied on real seawater, salts hang at the edge owing to other ions interferences (Figure S13I). Therefore, we remove Mg^{2+} by adjusting the pH to 12 and further Ca^{2+} by adding Na_2CO_3 to precipitate $CaCO_3$ ($Ksp = 4.8 \times 10^{-9}$), filtering the solution, then adjusting the pH back to 7 (Figure S14), and achieve continuous operation of the SVG and salt harvesting for 100 h (Figure 6B). Owing to the existence of Ca^{2+} and Mg^{2+}, a salt ring is formed around the evaporation surface in the first 10 h, which decreases the evaporation rate. As the evaporation continues, the salt ring moves gradually further beyond the edge and finally falls down by gravity, which triggers an increase in the evaporation rate. Afterward, the remaining seed crystals at the edge drive the salts to grow in a spatially isolating way instead of forming a ring again to keep the evaporation rate steady. After solar desalination, the ionic concentration (1.91 mg/L total dissolved solids) decreased far below the WHO drinking water standard (<1,000 mg/L, Figure 6C).

Ca^{2+} and Mg^{2+} can also decrease the mobility of the salt on the evaporation surface owing to their higher ionic potential, which indicates the surface charge density of an ion (Table S7). Ions with higher ionic potential attract more strongly opposite ions around. At the same time, Ca^{2+} and Mg^{2+} (especially Mg^{2+}) have the smallest diameters in the system (Table S7), making them easier to migrate into the NaCl precipitations and link the precipitations to make them bond stronger,[45,46] which decreases the mobility of the salt and makes the salt cover the surface gradually to the center (Figure 6D). Lower Ca^{2+} and Mg^{2+} concentrations make it possible

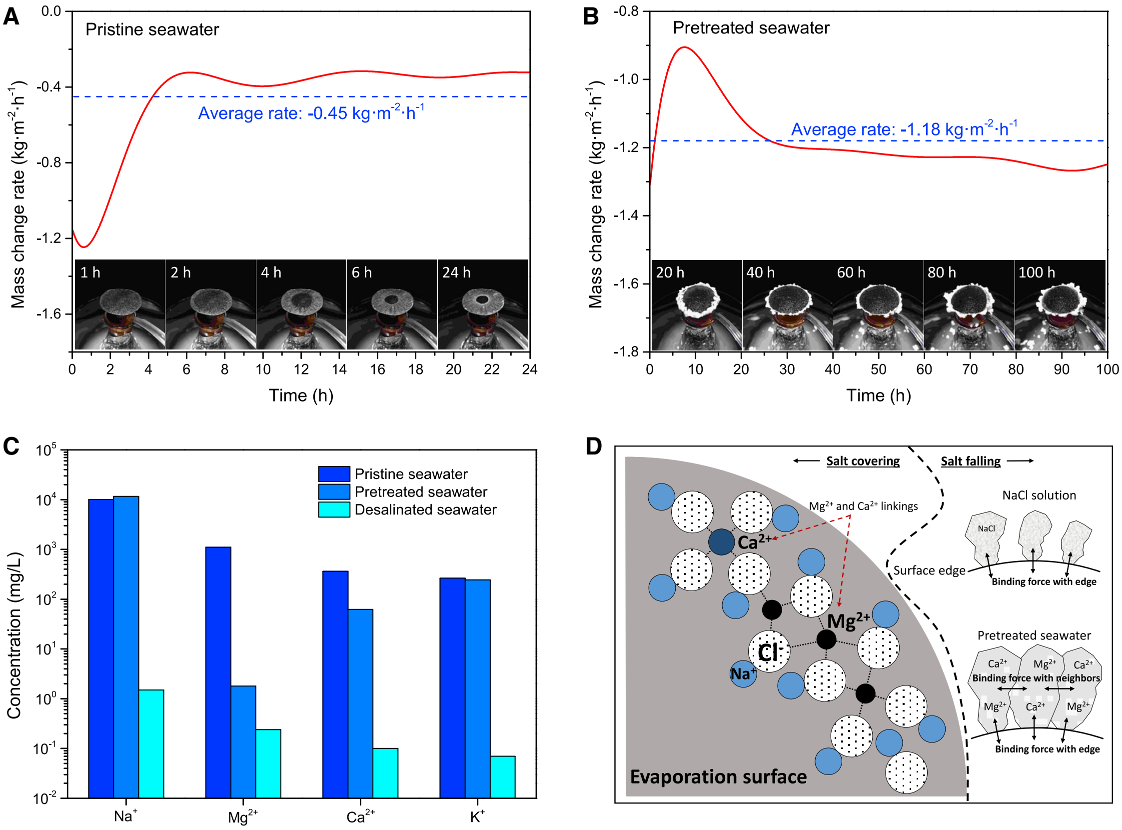

Figure 6. UE application on real seawater from Edinburgh Portobello Beach, UK

(A) Application on pristine seawater.

(B) Application on pretreated seawater.

(C) Ionic concentrations of pristine, pretreated, and desalinated seawater.

(D) Salt covering and falling mechanism schematic for real seawater.

to precipitate at the edge; however, their existence also affects the salt falling. Owing to the linking of Ca^{2+} and Mg^{2+} ions, the salts hanging on the edge become bigger and harder, and even bind with their neighbors, making it more difficult for them to fall (Figure 6D), which explains the formation of the salt ring at the beginning in Figure 6B.

Facile test for salt harvesting

The pretreated seawater quality (Mg^{2+} and Ca^{2+} content) determines if salts can be harvested from the edge. Knowing the ion contents usually requires professional equipment (e.g., inductively coupled plasma mass spectrometry or with an atomic absorption spectrophotometer [AAS]). Here, we establish a facile method to test if the pretreated seawater is satisfied for salt harvesting by simply dipping a drop on a glass slide. When the drop is naturally dry, the salt creeping that can be seen by the naked eye indicates the possibility of salt falling. Salt creeping is a common phenomenon that salt precipitates far from the evaporation boundary.[47] NaCl solution has typical salt creeping behavior (Figure 7A; Video S3), with fine crystals spreading out from the boundary. The pretreated seawater has a similar behavior as observed by naked eyes; however, at the micro level, the distance among crystals is closer with a top covering (Figure 7B). There is no such salt creeping behavior for pristine seawater (Figure 7C). More supporting figures for this phenomenon are in Figure S15.

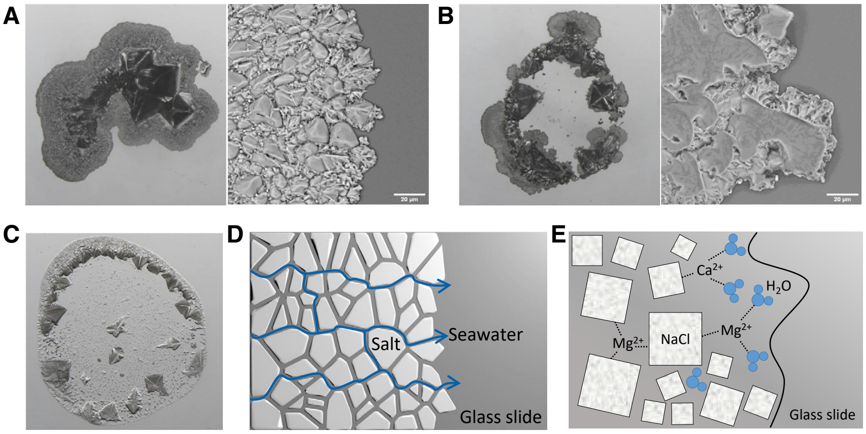

Figure 7. Salt creeping phenomenon for salt harvesting test
(A) Salt creeping of NaCl solution (3.5 wt %).
(B) Salt creeping of the pretreated seawater.
(C) Pristine seawater.
(D) Salt creeping mechanism schematic.
(E) Schematic of the restraining salt creeping by Ca^{2+} and Mg^{2+}. All the salt stains were created by dipping 20 μm salt water on a glass slide and naturally drying.

For salt creeping behavior, salt at the boundary forms many scattered crystals in a planar way at the end of drying, leaving channels between them to transport water to the frontline by capillary force (Figure 7D). When the content of Ca^{2+} and Mg^{2+} is high, owing to their greater ionic potential, they would link the water with salts to prevent the water from flowing forward instead of forming the salt creeping pattern (Figure 7E). Therefore, we can determine if the Ca^{2+} and Mg^{2+} content is low enough for UE salt harvesting by observing the salt creeping. Overall, the more obvious the salt creeping phenomenon, the easier it is for the salt to fall for harvesting.

In summary, we demonstrated an innovative UE and showed its structural advantages in SVG over a typical IE by both experiments and simulation, which is due to its double-sided evaporation feature, leading to a higher evaporation rate, i.e., 13.6% increase under 1 sun, and a higher energy efficiency. The UE is capable of continuous vapor and salt production concurrentlyfrom water containing up to 7 wt % of salt. Salt accumulation on the evaporation surface is a dynamic equilibrium of crystallization and dissolution, in which way salt moves to the edge. The mobility of the salt determines whether the salt can accumulate at the edge and fall. An insufficient water supply, high solar intensity, high salinity, and the presentation of Mg^{2+} (especially) and Ca^{2+} all decrease the salt's mobility, leading to gradual precipitation toward the center. The salt on the edge grows from the front by wicking the water through its porous structures inside and falls owing to the dissolution of its connecting parts. By removing Mg^{2+} and Ca^{2+} through sedimentations, we achieved continuous SVG with salt harvesting from real seawater for 100 h. Finally, we proposed a facile method to determine the water quality for salt harvesting by simply dipping a drop on a glass slide to observe the salt creeping behaviors: the stronger the salt creeping phenomenon, the easier it is for the salt harvesting.

EXPERIMENTAL PROCEDURES

Resource availability

Lead contact

Further information and requests for resources should be directed to and will be fulfilled by the Lead Contact, Dongsheng Wen (d.wen@buaa.edu.cn; d.wen@leeds.ac.uk).

Materials availability

This study did not generate new unique reagents or materials.

Data and code availability

Raw data are available from the lead contact upon reasonable request.

Assembly of the solar evaporators

Polypyrrole was coated on a filter paper to make the black solar evaporation surface for both the IE and UE, and the detailed coating method can be found in our previous work.[48] The solar evaporation surface diameter for both IE and UE is 3 cm. For the IE, a polystyrene foam (1.5 cm in thickness and 5 cm in diameter) was applied to act as the thermal insulation layer. For the UE, a polyester pillar (0.8 cm in diameter) was applied for water transportation.

Evaporation experiments

The simulated solar light was provided by a xenon arc lamp from a solar simulator (ORIEL Sol3ATM CLASS AAA SOLAR SIMULATOR) with an optical filter for air mass 1.5 global (AM 1.5 G) standard spectrum. The mass change was recorded every second by an analytical balance (Discovery DV144C Ohaus Corporation with a sensitivity of 0.1 mg) connecting to a computer for real-time monitoring. The laboratory was kept closed and quiet during the test and the samples were surrounded by a tin foil to minimize additional energy input into the system.

Characterization

The reflectance and transmittance spectra were measured by ultraviolet-visible-near-infrared spectrometer (PerkinElmer Lambda 950) with a 60-mm integrating sphere (PerkinElmer). The surface temperature was measured by FLIR ONE infrared camera (sensitivity of 0.1°C). The salt accumulation and salt creeping behaviors were recorded by a CCD camera (FLIR Grasshopper3 USB3, Model: GS3-U3-12S5C-C) mounted on a stereo microscope (Olympus, SZX16). The microstructures of the salt clusters were captured by Hitachi TM3030Plus SEM The ion concentration was measured by an AAS (Agilent Technologies, 200 Series AA).

Calculation of the energy efficiency

The solar thermal conversion efficiency was calculated by the following equation[49]:

$$\eta = \frac{m\left[Cp_{water}(T - T_0) + H_{LV}\right]}{E_{input}} \times 100\%. \qquad \text{(Equation 1)}$$

Here, m is the evaporation rate ($\mathrm{kg \cdot m^{-2} \cdot h^{-1}}$), E_{input} is the normal direct solar irradiation input (1,000 $\mathrm{W\,m^{-2}}$), Cp_{water} is the water specific heat capacity (4.2 $\mathrm{kJ\,kg^{-1} \cdot K^{-1}}$ at 1 atm), T and T_0 are the surface average temperature and initial temperature of water, respectively, and H_{LV} is the water enthalpy of vaporization at the surface equilibrium average temperature (2,420.8 kJ/kg at 33.8°C) (data from The Engineering ToolBox 2010 Water – Heat of Vaporization: https://www.engineeringtoolbox.com/water-properties-d_1573.html).

SUPPLEMENTAL INFORMATION

Supplemental information can be found online at https://doi.org/10.1016/j.xcrp.2022.100940.

ACKNOWLEDGMENTS

The authors appreciate financial support from China Scholarship Council and the European Research Council (ERC-2014-CoG, Project reference: 648375).

AUTHOR CONTRIBUTIONS

X.M. conducted the experiments, performed initial data analysis and wrote the manuscript draft. X.J. and G.Y. participated in the analysis and interpretation of the results. D.W. supervised the project and revised the manuscript draft.

DECLARATION OF INTERESTS

The authors declare no competing interests.

Received: March 25, 2022
Revised: April 25, 2022
Accepted: May 23, 2022
Published: June 15, 2022

REFERENCES

1. World Health Organization (2019). 1 in 3 people globally do not have access to safe drinking water – UNICEF, WHO. World Health Organization, June 18, 2019. https://www.who.int/news/item/18-06-2019-1-in-3-people-globally-do-not-have-access-to-safe-drinking-water-unicef-who.
2. Schlosser, C.A., Strzepek, K., Gao, X., Fant, C., Blanc, E., Paltsev, S., Jacoby, H., Reilly, J., and Gueneau, A. (2014). The future of global water stress: an integrated assessment. Earth's Future *2*, 341–361. https://doi.org/10.1002/2014ef000238.
3. Wu, L., Dong, Z., Cai, Z., Ganapathy, T., Fang, N.X., Li, C., Yu, C., Zhang, Y., and Song, Y. (2020). Highly efficient three-dimensional solar evaporator for high salinity desalination by localized crystallization. Nat. Commun. *11*, 521–532. https://doi.org/10.1038/s41467-020-14366-1.
4. Zhao, F., Zhou, X.Y., Shi, Y., Qian, X., Alexander, M., Zhao, X.P., Mendez, S., Yang, R.G., Qu, L.T., and Yu, G.H. (2018). Highly efficient solar vapour generation via hierarchically nanostructured gels. Nat. Nanotechnol. *13*, 489–495. https://doi.org/10.1038/s41565-018-0097-z.
5. Wen, B.Y., Zhang, X.Y., Yan, Y.H., Huang, Y.Q., Lin, S., Zhu, Y.L., Wang, Z.P., Zhou, B.H., Yang, S.H., and Liu, J. (2021). Tailoring polypyrrole-based janus aerogel for efficient and stable solar steam generation. Desalination *516*, 115228–115237. https://doi.org/10.1016/j.desal.2021.115228.
6. Zang, L.L., Finnerty, C., Zheng, S.X., Conway, K., Sun, L.G., Ma, J., and Mi, B.X. (2021). Interfacial solar vapor generation for desalination and brine treatment: evaluating current strategies of solving scaling. Water Res. *198*, 117135. https://doi.org/10.1016/j.watres.2021.117135.
7. Zhou, L., Li, X.Q., Ni, G.W., Zhu, S.N., and Zhu, J. (2019). The revival of thermal utilization from the Sun: interfacial solar vapor generation. Natl. Sci. Rev. *6*, 562–578. https://doi.org/10.1093/nsr/nwz030.
8. Li, Y.X., Chen, H.W., Xiao, S.Y., Alibakhshi, M.A., Lo, C.W., Lu, M.C., and Duan, C.H. (2019). Ultrafast diameter-dependent water evaporation from nanopores. ACS Nano *13*, 3363–3372. https://doi.org/10.1021/acsnano.8b09258.
9. Zhao, F., Guo, Y., Zhou, X., Shi, W., and Yu, G. (2020). Materials for solar-powered water evaporation. Nat. Rev. Mater. *5*, 388–401. https://doi.org/10.1038/s41578-020-0182-4.
10. Li, X., Guan, C., Gao, X., Zuo, X., Yang, W., Yan, H., Shi, M., Li, H., and Sain, M. (2020). High efficiency solar membranes structurally designed with 3D core-2D shell SiO2@Amino-carbon hybrid advanced composite for facile steam generation. ACS Appl. Mater. Inter. *12*, 35493–35501. https://doi.org/10.1021/acsami.0c10461.
11. Guo, X.X., Gao, H., Wang, S.Y., Yin, L.F., and Dai, Y.R. (2020). Scalable, flexible and reusable graphene oxide-functionalized electrospun nanofibrous membrane for solar photothermal desalination. Desalination *488*, 114535–114543. https://doi.org/10.1016/j.desal.2020.114535.
12. Guan, W.X., Guo, Y.H., and Yu, G.H. (2021). Carbon materials for solar water evaporation and desalination. Small *17*, 2007176. https://doi.org/10.1002/smll.202007176.
13. Cao, S.S., Jiang, Q.S., Wu, X.H., Ghim, D., Gholami Derami, H., Derami, H.G., Chou, P.I., Jun, Y.S., and Singamaneni, S. (2019). Advances in solar evaporator materials for freshwater generation. J. Mater. Chem. *7*, 24092–24123. https://doi.org/10.1039/c9ta06034k.
14. Liu, G.H., Xu, J.L., and Wang, K.Y. (2017). Solar water evaporation by black photothermal sheets. Nano Energy *41*, 269–284. https://doi.org/10.1016/j.nanoen.2017.09.005.
15. Liu, G.H., Chen, T., Xu, J.L., Li, G., and Wang, K.Y. (2020). Solar evaporation for simultaneous steam and power generation. J. Mater. Chem. *8*, 513–531. https://doi.org/10.1039/c9ta12211g.
16. Jin, H.C., Lin, G.P., Bai, L.Z., Zeiny, A., and Wen, D.S. (2016). Steam generation in a nanoparticle-based solar receiver. Nano Energy *28*, 397–406. https://doi.org/10.1016/j.nanoen.2016.08.011.
17. Ghasemi, H., Ni, G., Marconnet, A.M., Loomis, J., Yerci, S., Miljkovic, N., and Chen, G. (2014). Solar steam generation by heat localization. Nat. Commun. *5*, 4449–4455. https://doi.org/10.1038/ncomms5449.
18. Xia, Y., Kang, Y., Wang, Z.Y., Yuan, S., Li, Y., Gao, L., Wang, H.T., and Zhang, X.W. (2021). Rational designs of interfacial-heating solar-thermal desalination devices: recent progress and remaining challenges. J. Mater. Chem. A *9*, 6612–6633. https://doi.org/10.1039/d0ta11911c.
19. Wang, P.F., Wang, X.Y., Chen, S.Y., Zhang, J.H., Mu, X.J., Chen, Y.L., Sun, Z.Q., Wei, A.Y., Tian, Y.Z., Zhou, J.H., et al. (2021). Reduced red mud as the solar absorber for solar-driven water evaporation and vapor-electricity generation. ACS Appl. Mater. Inter. *13*, 30556–30564. https://doi.org/10.1021/acsami.1c05228.
20. Yang, Y.W., Que, W.X., Zhao, J.Q., Han, Y., Ju, M.M., and Yin, X.T. (2019). Membrane assembled from anti-fouling copper-zinc-tin-selenide nanocarambolas for solar-driven interfacial water evaporation. Chem. Eng. J. *373*, 955–962. https://doi.org/10.1016/j.cej.2019.05.099.
21. Kashyap, V., Al-Bayati, A., Sajadi, S.M., Irajizad, P., Wang, S.H., and Ghasemi, H. (2017). A flexible anti-clogging graphite film for scalable solar desalination by heat localization. J. Mater. Chem. A *5*, 15227–15234. https://doi.org/10.1039/c7ta03977h.
22. Liu, G.H., Chen, T., Xu, J.L., Yao, G.S., Xie, J., Cheng, Y.P., Miao, Z., and Wang, K.Y. (2021). Salt-rejecting solar interfacial evaporation. Cell Reports Physical Science *2*, 100310. https://doi.org/10.1016/j.xcrp.2020.100310.
23. Zhang, C., Liang, H.Q., Xu, Z.K., and Wang, Z.K. (2019). Harnessing solar-driven photothermal effect toward the water-energy nexus. Adv. Sci. *6*, 1900883. https://doi.org/10.1002/advs.201900883.
24. Kuang, Y.D., Chen, C.J., He, S.M., Hitz, E.M., Wang, Y.L., Gan, W.T., Mi, R.Y., and Hu, L.B. (2019). A high-performance self-regenerating solar evaporator for continuous water desalination. Adv. Mater. *31*, 1900498. https://doi.org/10.1002/adma.201900498.
25. Zhang, Q., Hu, R., Chen, Y.L., Xiao, X.F., Zhao, G.M., Yang, H.J., Li, J.H., Xu, W.L., and Wang, X.B. (2020). Banyan-inspired hierarchical evaporators for efficient solar photothermal

conversion. Appl. Energy *276*, 115545. https://doi.org/10.1016/j.apenergy.2020.115545.

26. Xu, Z., Zhang, L., Zhao, L., Li, B., Bhatia, B., Wang, C., Wilke, K.L., Song, Y., Labban, O., Lienhard, J.H., et al. (2020). Ultrahigh-efficiency desalination via a thermally-localized multistage solar still. Energy Environ. Sci. *13*, 830–839. https://doi.org/10.1039/c9ee04122b.

27. Ni, G., Zandavi, S.H., Javid, S.M., Boriskina, S.V., Cooper, T.A., and Chen, G. (2018). A salt-rejecting floating solar still for low-cost desalination. Energy Environ. Sci. *11*, 1510–1519. https://doi.org/10.1039/c8ee00220g.

28. Zhang, Q., Yang, H.J., Xiao, X.F., Wang, H., Yan, L., Shi, Z.X., Chen, Y.L., Xu, W.L., and Wang, X.B. (2019). A new self-desalting solar evaporation system based on a vertically oriented porous polyacrylonitrile foam. J. Mater. Chem. *7*, 14620–14628. https://doi.org/10.1039/c9ta03045j.

29. Xu, W.C., Hu, X.Z., Zhuang, S.D., Wang, Y.X., Li, X.Q., Zhou, L., Zhu, S.N., and Zhu, J. (2018). Flexible and salt resistant janus absorbers by electrospinning for stable and efficient solar desalination. Adv. Energy Mater. *8*, 1702884. https://doi.org/10.1002/aenm.201702884.

30. Zhou, X.Y., Zhao, F., Guo, Y.H., Zhang, Y., and Yu, G.H. (2018). A hydrogel-based antifouling solar evaporator for highly efficient water desalination. Energy Environ. Sci. *11*, 1985–1992. https://doi.org/10.1039/c8ee00567b.

31. Menon, A.K., Haechler, I., Kaur, S., Lubner, S., and Prasher, R.S. (2020). Enhanced solar evaporation using a photo-thermal umbrella for wastewater management. Nat. Sustain. *3*, 144–151. https://doi.org/10.1038/s41893-019-0445-5.

32. Zhang, L.N., Li, X.Y., Zhong, Y., Leroy, A., Xu, Z.Y., Zhao, L., and Wang, E.N. (2022). Highly efficient and salt rejecting solar evaporation via a wick-free confined water layer. Nat. Commun. *13*, 849. https://doi.org/10.1038/s41467-022-28457-8.

33. Xia, Y., Li, Y., Yuan, S., Kang, Y., Jian, M.P., Hou, Q.F., Gao, L., Wang, H.T., and Zhang, X.W. (2020). A self-rotating solar evaporator for continuous and efficient desalination of hypersaline brine. J. Mater. Chem. *8*, 16212–16217. https://doi.org/10.1039/d0ta04677a.

34. Finnerty, C., Zhang, L., Sedlak, D.L., Nelson, K.L., and Mi, B.X. (2017). Synthetic graphene oxide leaf for solar desalination with zero liquid discharge. Environ. Sci. Technol. *51*, 11701–11709. https://doi.org/10.1021/acs.est.7b03040.

35. Shi, Y., Zhang, C.L., Li, R.Y., Zhuo, S.F., Jin, Y., Shi, L., Hong, S., Chang, J., Ong, C.S., and Wang, P. (2018). Solar evaporator with controlled salt precipitation for zero liquid discharge desalination. Environ. Sci. Technol. *52*, 11822–11830. https://doi.org/10.1021/acs.est.8b03300.

36. Xia, Y., Hou, Q.F., Jubaer, H., Li, Y., Kang, Y., Yuan, S., Liu, H.Y., Woo, M.W., Zhang, L., Gao, L., et al. (2019). Spatially isolating salt crystallisation from water evaporation for continuous solar steam generation and salt harvesting. Energy Environ. Sci. *12*, 1840–1847. https://doi.org/10.1039/c9ee00692c.

37. Chen, X.X., Wu, Z.Y., Lai, D.G., Zheng, M., Xu, L., Huo, J.B., Chen, Z.X., Yuan, B.L., and Fu, M.L. (2020). Resilient biomass-derived hydrogel with tailored topography for highly efficient and long-term solar evaporation of high-salinity brine. J. Mater. Chem. *8*, 22645–22656. https://doi.org/10.1039/d0ta07040h.

38. Shao, Y., Tang, J.B., Li, N.B., Sun, T.Y., Yang, L.P., Chen, D., Zhi, H., Wang, D.J., Liu, H., and Xue, G.B. (2020). Designing a bioinspired synthetic tree by unidirectional freezing for simultaneous solar steam generation and salt collection. Ecomat *2*, e12018. https://doi.org/10.1002/eom2.12018.

39. Peng, H.Y., Wang, D., and Fu, S.H. (2021). Artificial transpiration with asymmetric photothermal textile for continuous solar-driven evaporation, spatial salt harvesting and electrokinetic power generation. Chem. Eng. J. *426*, 131818. https://doi.org/10.1016/j.cej.2021.131818.

40. Li, X.Q., Li, J.L., Lu, J.Y., Xu, N., Chen, C.L., Min, X.Z., Zhu, B., Li, H.X., Zhou, L., Zhu, S.N., et al. (2018). Enhancement of interfacial solar vapor generation by environmental energy. Joule *2*, 1331–1338. https://doi.org/10.1016/j.joule.2018.04.004.

41. Tao, P., Ni, G., Song, C., Shang, W., Wu, J., Zhu, J., Chen, G., and Deng, T. (2018). Solar-Driven interfacial evaporation. Nat. Energy *3*, 1031–1041. https://doi.org/10.1038/s41560-018-0260-7.

42. Davenport, D.M., Deshmukh, A., Werber, J.R., and Elimelech, M. (2018). High-pressure reverse osmosis for energy-efficient hypersaline brine desalination: current status, design considerations, and research needs. Environ. Sci. Technol. Lett. *5*, 467–475. https://doi.org/10.1021/acs.estlett.8b00274.

43. Voorhees, P.W. (1985). The theory of ostwald ripening. J. Stat. Phys. *38*, 231–252. https://doi.org/10.1007/bf01017860.

44. Veran-Tissoires, S., Marcoux, M., and Prat, M. (2012). Discrete salt crystallization at the surface of a porous medium. Phys. Rev. Lett. *108*, 054502. https://doi.org/10.1103/physrevlett.108.054502.

45. Underwood, T., Erastova, V., Cubillas, P., and Greenwell, H.C. (2015). Molecular dynamic simulations of montmorillonite organic interactions under varying salinity: an insight into enhanced oil recovery. J. Phys. Chem. C *119*, 7282–7294. https://doi.org/10.1021/acs.jpcc.5b00555.

46. Wang, J.Y., Bai, Y., Sui, H., Li, X.G., and He, L. (2021). Understanding the effects of salinity on bitumen-calcite interactions. Fuel Process. Technol. *213*, 106668. https://doi.org/10.1016/j.fuproc.2020.106668.

47. Qazi, M.J., Salim, H., Doorman, C.A.W., Jambon-Puillet, E., and Shahidzadeh, N. (2019). Salt creeping as a self-amplifying crystallization process. Sci. Adv. *5*, eaax1853. https://doi.org/10.1126/sciadv.aax1853.

48. Ma, X., Jia, X., Gao, H., and Wen, D. (2021). Polypyrrole–dopamine nanofiber light-trapping coating for efficient solar vapor generation. ACS Appl. Mater. Inter. *13*, 57153–57162. https://doi.org/10.1021/acsami.1c17249.

49. Li, X., Ni, G., Cooper, T., Xu, N., Li, J., Zhou, L., Hu, X., Zhu, B., Yao, P., and Zhu, J. (2019). Measuring conversion efficiency of solar vapor generation. Joule *3*, 1798–1803. https://doi.org/10.1016/j.joule.2019.06.009.